Reviews of Electromagnetics, Vol. IV, 2025
EuCAP 2025 Special Issue
DOI: 10.53792/RoE/2025/25001

Reviews of Electromagnetics
EuCAP 2025 Special Issue

A Scalable Differential Series-fed Dipole Array for D-band Radar in Wafer-Level Package Technology

Martijn de Kok[1]*, Paola A. Escobari Vargas[1], Elmine Meyer[1], Friedrich Müller[2], Tanja Braun[2], Ad C. F. Reniers[1], and Ulf Johannsen[1]

Abstract
This article presents the design and characterization of a scalable series-fed differential Antenna-in-Package (AiP) design, demonstrated as a four- and a six-element reflector-backed linear dipole array that has been realized in a resin-based fan-out wafer-level package technology. The simulated four- and six-element designs achieve -10 dB input reflection bandwidths of 5.5 and 5.9 percent, realized gains of 14 and 15.4 dBi, and side-lobe levels of -10.7 and -12.1 dB, respectively. Frequency scanning is limited to $\pm 4^\circ$ throughout the bandwidth for both designs. The realized samples were characterized through probed measurements in a state-of-the-art millimeter-wave anechoic chamber. After taking into account the influence of the RF probe on antenna performance, the measurements corroborated the simulated results. The presented designs represent a beyond-state-of-the-art contribution in gain-to-area ratio to the currently limited number of high-gain differential AiPs at D-band found in literature. This article expands upon a 2025 EuCAP paper with more detailed descriptions, a scalability study, and a simulated feasibility demonstration of a scanning array implementation for further gain enhancement and a $\pm 45^\circ$ scan range.

Key terms
Antenna-in-package; Differential antenna; Reflector-backed dipole; Fan-out wafer level package; D-band; millimeter-Wave; Antenna measurement

[1] *Department of Electrical Engineering, Eindhoven University of Technology, Eindhoven, The Netherlands*
[2] *Department of System Integration & Interconnection Technologies, Fraunhofer IZM, Berlin, Germany*
***Corresponding author**: m.d.kok@tue.nl*

Received: 28/03/2025, Accepted: 20/07/2025, Published: 28/11/2025

1. Introduction

In pursuit of increased performance and wider available bandwidths in the densely allocated radio frequency (RF) spectrum, developments of wireless communication and sensing devices are pushing towards increasingly higher frequencies within the millimeter-wave (mm-wave) band between 30 and 300 GHz. For communication applications, the high-volume backhaul capabilities of the D-band (110-170 GHz) are promising for the dense mobile networks envisioned for 5G and beyond [1]. Sensing devices beyond 100 GHz, most notably short-range radars operating in the 122 GHz industrial, scientific and medical (ISM)-band, can already be found in literature [2, 3]. In addition, researchers and industry are already looking towards D-band radar as a successor to the 77 GHz devices that are now solidly established in the automotive sector [4, 5].

The difficulty and cost of generating high-power RF signals increase with frequency, and so do propagation losses in air, transmission lines, and interconnects. One of the key challenges in mm-wave antenna design is to optimize the antenna efficiency and limiting interconnect losses through the use of low-loss materials and close integration between the antenna and active electronics. In the D-band, the antennas can be small enough to be implemented within the same package as the RF integrated circuits (ICs). The benefits of such an Antenna-in-Package (AiP) design include reduced size, interconnect losses, and system assembly costs. Moreover, such a module only requires a power supply and baseband signals at its interface, limiting high-performance materials and high-complexity mm-wave design efforts to within the module to achieve system-level cost savings and faster time to market.

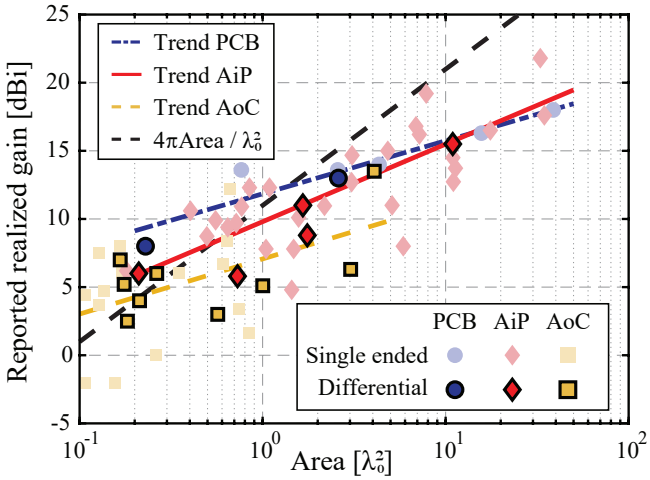

Figure 1: Overview of reported realized gain performances of D-band PCB, package and chip-based antennas from literature. Adapted from [6] and expanded with recent works: [7–15]. All differential designs are outlined. λ_0 denotes the center frequency free-space wavelength.

In Fig. 1, based on a review study presented in [6], an overview is shown of the reported realized gain-area performances of antennas integrated on printed circuit board (PCB), in-package, and on-chip. Although Antenna-on-Chip (AoC) designs offer the highest level of antenna-circuit integration, high manufacturing resolutions, and micrometer-level tolerances, advanced post-processing techniques are often required to achieve acceptable radiation efficiencies as described in the review. Moreover, the scalability of AoCs to high-gain designs is limited by expensive surface area of mm-wave IC technologies. Only a small number of AoCs in Fig. 1 exceed a squared wavelength in size, roughly translating to 4 mm^2 of dedicated chip area at D-band. As a result, the design space of $\geq$10 dBi and $\geq \lambda_0^2$-sized integrated antennas at D-band is dominated by AiP designs, as illustrated in Fig. 1. In [6], AiPs based on integrated substrates, low-temperature co-fired ceramics (LTCC), and organic redistribution layer (RDL) technologies were concluded to outperform PCB-based and on-chip antennas in terms of efficiency and scalability.

Manufacturing technologies are pivotal for the realization of efficient mm-wave AiPs. Tolerances need to be tight given the small antenna dimensions, and both electrical and mechanical material properties must be well-characterized to mitigate frequency offsets and deformities. In this work a fan-out wafer-level package (FOWLP) technology from Fraunhofer Institute for Reliability and Microintegration (IZM) is demonstrated, which achieves better tolerances than the LTCC-based antennas listed in [6] whilst enabling multi-layer designs as opposed to other RDL-technologies as shown in Fig. 2 [16]. This technology has already enabled 5G and beyond-5G antennas in the mm-wave bands [7, 17], and is described in more detail in the next section.

This publication presents two 110 GHz differential reflector-backed dipole arrays, which were designed and characterized as part of the Eindhoven University of Technology (TU/e) goals of realizing antennas and circuit components for the next generation of automotive radars operating beyond 100 GHz [5]. The differential circuits in development have several valuable advantages over single-ended designs, including simplified layout design due to the virtual ground, lower signal distortion, suppression of interference signals and common-mode noise, and better power efficiency due to the doubled maximum voltage swing [18, 19]. Differential AiPs complement this by enabling close integration without the area and power loss of a balancing unit (balun). However, differential antennas at D-band, particularly high-gain AiP designs, are uncommon to find in published literature as illustrated by their limited representation in Fig. 1.

The presented series-fed antenna arrays demonstrate excellent radiation efficiencies and high-gain fan-shaped beams with limited squint, as is presented in Section 3. The novel FOWLP-based designs represent a contribution beyond the state of the art, achieving a better gain-to-surface ratio than the severely limited number of high-gain differential AiPs in the D band found in the literature.

An earlier version of this paper was presented at the 2025 19th European Conference on Antennas and Propagation (EuCAP) and was published in its Proceedings [20]. This is an extension of the work and includes the following novel additions. Firstly, an in-depth examination of the gain, efficiency and bandwidth scalability of the series-fed array has been performed. This analysis is presented in Section 3-C. Secondly, the realized gain performance and beam offset of the measured antennas are examined, with the results shown in Section 5-C. Thirdly, a new array configuration is examined as a feasibility study in Section 6, showing the potential for further improved gain and angular resolution as well as electronic scanning in contrast to earlier D-band AiPs [2, 21]. Moreover, this expanded version contains a more detailed description of the mm-wave measurement setups including the anechoic chamber and the limitations of probe measurements. It also provides a more in-depth analysis of the simulated and measured performance, and presents measured impedances, far-field patterns, and trueness results in Section 5 which were previously omitted for brevity.

The realized antennas were characterized using probe-based over-the-air (OTA) measurement techniques. A state-of-the-art mm-wave anechoic chamber, previously developed in-house at TU/e, was used in this process [22]. The measurement procedure and the effects of the RF-probe on the measured radiation patterns are described in more detail in Section 4. The measurement results are presented and discussed in Section 5 including a comparison against state-of-the-art examples, and Section 7 concludes this paper.

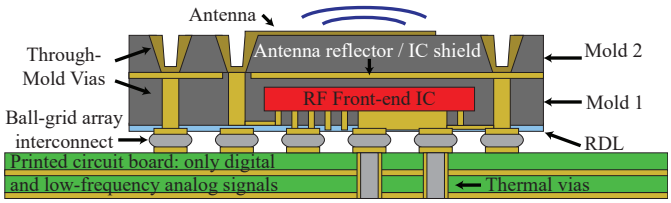

Figure 2: Concept illustration of a FOWLP-based AiP integrated with an RF IC as a single module, based on [17].

Table 1: Typical manufacturing parameters and tolerances without optimization for direct metallization on encapsulants

Dimension	Value [μm]	Tolerance [±μm]
Substrate thickness	250	10
Copper thickness	10	2
Via placement	–	25
Etching accuracy: traces	≥ 25	10
Etching accuracy: gaps	≥ 50	10

2. Fan-out Wafer Level Package Technology

FOWLP integrates multiple ICs by wafer-level encapsulation, forming a reconfigured wafer. A redistribution layer is then used to connect the ICs. The active area of the package extends beyond the dies, facilitating an increased number of interconnects and embedded passive components [23].

Fraunhofer IZM has developed a technique to stack multiple metallized mold layers, to realize advanced RDLs, electromagnetic shielding, and multilayer antennas that are located directly above the RF IC and the encapsulant to reduce the module surface area, as illustrated in Fig. 2. The sputter-coated and electroplated metallization layers are connected with laser-drilled through-mold vias or slots. The technology and manufacturing steps are described in detail in [17]. An overview of typical manufacturing parameters for direct metallization on the encapsulant, including design rules and tolerances, is provided in Table 1. The minimum allowed trace widths and gaps are less than half the size of conventional PCB technologies, enabling the design of compact differential lines and antennas.

In this work, only a single mold layer with bottom- and top-side metallization is considered to realize a passive demonstrator without an active chip. In Fig. 2, this is indicated as 'Mold 2'. The vertical interconnect to feed the antenna is not considered to facilitate probe measurements. The antenna samples were manufactured alongside a variety of other sample structures, including mm-wave antennas and material characterization structures that are part of ongoing research. This predetermined the outer dimensions of 25×25 mm^2 and substrate thickness of 250 μm.

All designs are produced on compression-molded circular resin wafers of 200 mm diameter, resulting in a total of 46 samples per wafer. The resin, which was characterized between 60 and 90 GHz using a Fabry-Pérot open resonator at TU/e, has a dielectric constant ε_r of 3.6 and a loss tangent ($\tan\delta$) of 0.0055 with a precision of 3% [24]. The substrate surface roughness can be influenced by the molding process and by post-processing, e.g. grinding and polishing. A total of six wafers with three sets of copper roughness profiles on the top and bottom sides were produced for a characterization study, although only two wafers with the smallest root mean square (RMS) roughness of approximately 0.55 μm at the antenna side were considered for this work.

3. Design and Realization

This section describes the design of the antenna elements, including the expected performance based on full-wave simulations in Dassault Systèmes' CST Studio Suite (CST) [25].

Table 2: Antenna requirements with links to radar performance

Specification	Requirement	Radar performance
Element x-dimension	$\leq \frac{1}{2}\lambda_0$	Prevent grating lobes
Element gain	≥ 15 dBi	Operating range
E-plane HPBW	$\geq 70°$	Scan range
H-plane HPBW	$\leq 12°$	Angular resolution
Bandwidth	$\geq 5\%$	Range resolution

3.1. Requirements

A fan-shaped element pattern with a high broadside gain is generally desired for automotive radar array applications. This enables a wide scan range in the azimuth plane, whilst focusing the radiated power in elevation, where a much narrower field of view is required. Typically, the required bandwidth is limited to around 5% of the center frequency, or 4 GHz at 79 GHz [26].

Hence, as a proof of concept design, a high-gain fan-shaped element pattern and relative bandwidth of 5% were taken as the principal design requirements for an automotive radar system beyond 100 GHz, as listed in Table 2. Series-fed antenna structures are typically capable of meeting both requirements, making them a popular choice in contemporary automotive radar systems and also interesting options for D-band applications [4, 7]. Although a 145 GHz design would have been preferred to align with the allocated radar band, the choice of 110 GHz as center frequency was based on the available laboratory equipment.

The antenna was specified to interface with mm-wave radar circuits in development at TU/e with a standard differential impedance of 100 Ω, eliminating the need for a lossy impedance transformer and balun between AiP and IC.

3.2. Design

At around 17% of a guided wavelength at 110 GHz, the predetermined substrate thickness of 250 μm was considered too thick for a microstrip-based antenna, helping with wide-band performance but reducing efficiency. Instead, the starting point of the proposed AiP was a scaled version of the dipole antenna presented in [27], where the bottom metalization acts as a reflector instead of a ground plane.

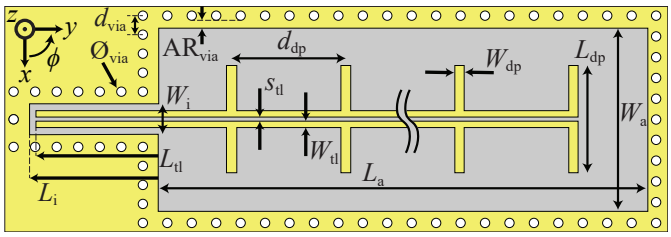

Figure 3: Illustration of the AiP simulation model, with the indicated variables representing the dimensions listed in Table 3. The antennas are centered on a 250 μm thick substrate which extends to 25×25 mm in all designs and models. A reflecting metal plane covers the entire bottom of the substrate.

Table 3: Antenna dimensions corresponding to Fig. 3

Dimension	Symbol	Value [µm]
Dipole length (x-dimension)	L_{dp}	1765
Dipole width (y-dimension)	W_{dp}	150
Dipole element spacing	d_{dp}	1865
Transmission line length	L_{tl}	2000
Transmission line conductor width	W_{tl}	100
Transmission line conductor gap	s_{tl}	70
Input aperture length	L_i	2100
Input aperture width	W_i	500
Aperture width	W_a	3000
Aperture length (4 elements)	L_{a4}	8000
Aperture length (6 elements)	L_{a6}	12000
Fence via spacing	d_{via}	310 – 400
Fence via diameter	$\varnothing_{via}$	150
Fence via annular ring	AR_{via}	125

The resulting design is presented in Fig. 3. A total of six reflector-backed dipole elements are placed in series, with the length and width of the elements tuned in CST to achieve a 100 Ω match at the center frequency of 110 GHz. The dipoles are approximately one guided wavelength λ_g long, exceeding the half-wavelength element size requirement specified in Table 2. However, this can be remedied by using a staggered array grid as will be demonstrated in Section 5-D.

The spacing of the elements d_{dp} at approximately one guided wavelength ensures that all elements radiate in phase at the center frequency, as illustrated in Fig. 4. A variety of visually similar designs operating at 28 GHz was presented by H. Wang et al in [28–30], although as a key difference it should be noted that these earlier designs radiate towards endfire due to the critically different reflector plane design. Radiation parallel to the board is generally undesired for PCB-mounted AiPs. In this work, the reflecting metal below the antenna results in a broadside beam perpendicular to the board surface, which is more suitable for a flat-panel array.

The antenna array is enclosed by a fence of through-mold vias to prevent the leaky wave contribution in the resin substrate from reaching the edge of the sample and causing spurious edge radiation. This fence was placed sufficiently far from the dipoles for the drilling tolerances to be negligible on the matching and

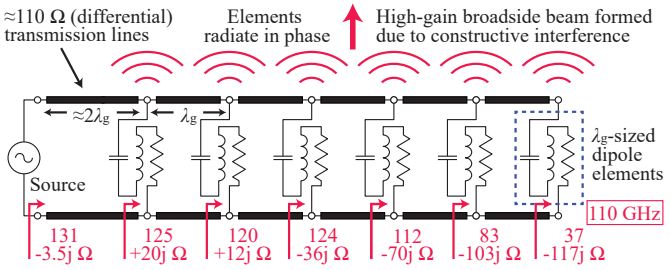

Figure 4: Circuit model to illustrate the working principle of the presented antenna. The dipole elements are represented by lossy resonant circuits. Intermediate interface impedances are given for the 6-element design at 110 GHz.

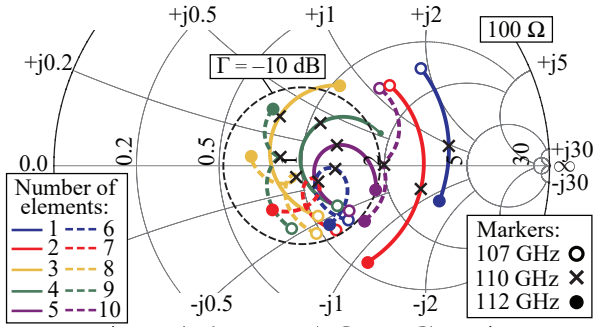

Figure 5: Simulated input reflection coefficients for 1 to 10 dipole elements, projected on a Smith chart (center is 100 Ω) between 107 and 112 GHz.

radiation, which was verified using simulations in CST.

3.3. Design scalability

Based on the interface impedances depicted in Fig. 4, an approximate −10 dB match is already achieved from three parallel elements and more. A series of design variations has been simulated, where the number of elements varies from 1 to 10 and only L_a is adjusted in millimeter increments to maintain a space between the antenna and the fence. From the simulated input reflection coefficients mapped to the Smith chart in Fig. 5, −10 dB matches are achieved with element counts between 3 and 9, with bandwidths of the order of at least 5 GHz.

By nature of the series-feed, an increased number of elements leads to a proportional increase in gain, a decrease in H-plane half-power beamwidth, and a reduction in achievable bandwidth [31]. Fig. 6 depicts this increase of peak realized gain versus the number of elements, and therefore the aperture area $W_a \times L_a$, for the ten simulated designs. The radiation efficiency η_{rad} decreases from 81 to 71% between 1 and 10 elements, as the transmission line losses increase with the number of elements. η_{rad} should not be confused with aperture efficiency η_a, which links the realized gain G_r with the physical aperture dimension A_{phys} [32]:

$$G_r = \eta_{rad}|1-\Gamma^2|D = \frac{4\pi A_e}{\lambda_0^2} = \frac{4\pi\eta_a A_{phys}}{\lambda_0^2} \quad (1)$$

Γ and D denote the antenna input reflection and directivity, respectively, and λ_0 is the free-space wavelength. As can be in-

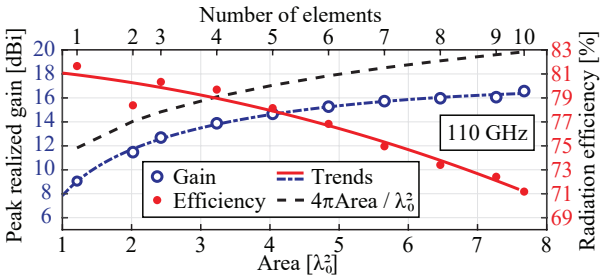

Figure 6: Simulated peak realized gain values and radiation efficiencies for 1 to 10 elements, versus area ($W_a \times L_a$) in wavelengths at 110 GHz.

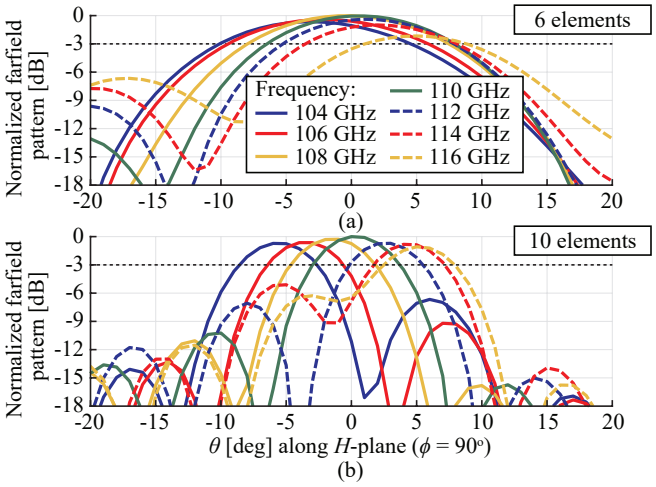

Figure 7: *H*-plane cuts of simulated realized-gain far field patterns of 6-element (a) and 10-element (b) designs, depicting the frequency squint effect between 104 and 116 GHz.

terpreted from Fig. 1, the effective aperture area A_e can exceed A_{phys}, resulting in a η_a of larger than unity. In particular, this can be the case for small antennas, thin wire antennas, and scenarios where structures near the antenna contribute to gain enhancement [32]. For higher-gain designs, an increasing G_r-trend that approximates the ideal $4\pi A_{phys}/\lambda_0$-line indicates efficient gain scalability with limited decrease of radiation efficiency.

The bandwidth reduction with element count is not necessarily related to the input reflection coefficient. A varying progressive phase shift will be induced by a change in signal frequency, which causes the main beam to steer somewhat throughout the bandwidth as is typical for this type of series-fed antenna. The amount of steering remains constant with element count, as this is a result of the interelement spacing and propagation constant. However, the narrower main beam of larger designs will move away from broadside within a narrower frequency span, as depicted in Fig. 7: the six-element design maintains a broadside gain reduction of less than 3 dB for nearly the entire 104-116 GHz simulation range, whereas the 10-element version is limited to 106-112 GHz. Although an edge-fed design was necessitated by the RF-probe measurements, a center-fed design could maintain a symmetric beam throughout the bandwidth. However, as such a design can be seen as two back-to-back edge-fed arrays that frequency-scan in opposite directions, it would still experience beam-broadening and gain reduction with frequency.

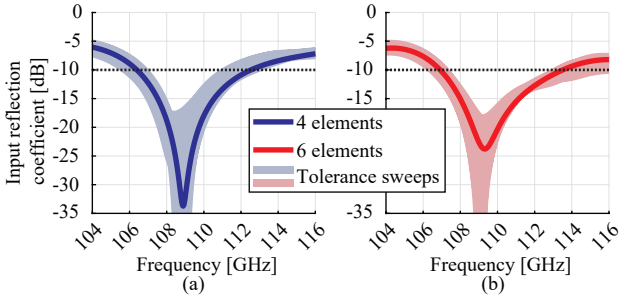

Figure 8: Simulated input reflection coefficients of the four-element (a) and six-element (b) designs, with the ranges indicating maximum variations due to manufacturing tolerances. Reference impedance: 100 Ω.

A four-element antenna was created to verify the scalability of the proposed design. This design was derived from the six-element version simply by removing two elements and reducing the aperture length L_a. No further matching or tuning was performed or required. The final antenna dimensions as depicted in Fig. 3 are listed in Table 3.

3.4. Simulated performance

The simulated input reflection coefficients of the four- and six-element antennas are depicted in Fig. 8. The robustness of the design against the etching, drilling, and substrate tolerances listed in Table 1 was assessed through a parameter sweep with the combinations of all extreme tolerance values. Based on nominal performance, the four- and six-element designs are expected to achieve −10 dB input reflection bandwidths of 6 and 6.5 GHz or 5.5% and 5.9%, respectively, achieving the 5% requirement with a margin. Variations due to tolerances indicate a possible shift in operating frequency limited to around ±0.5 GHz, or ±0.5%. A bow-tie-shaped element could be chosen instead of the straight dipole to achieve a slightly wider bandwidth, although this was not considered as the specified bandwidth requirement was already met.

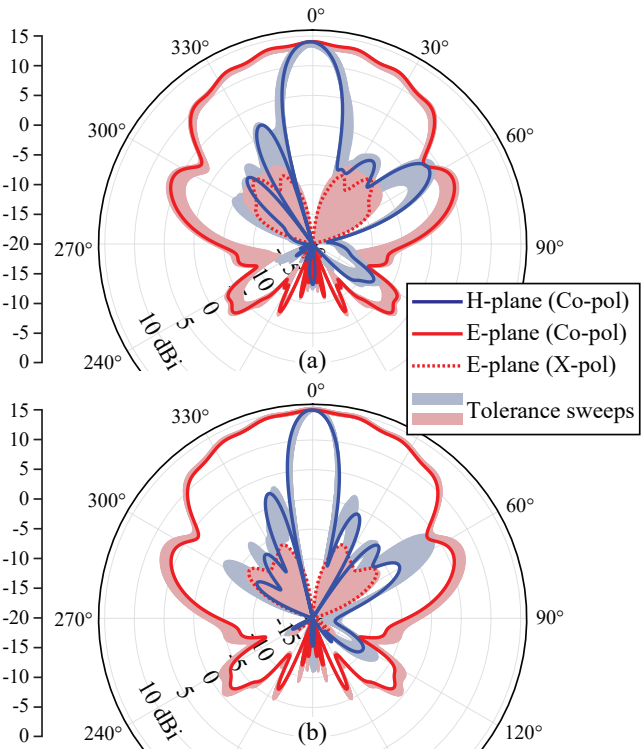

Figure 9: Simulated realized-gain farfield patterns of the four-element (a) and six-element (b) designs at 110 GHz, with the ranges indicating maximum variations due to manufacturing tolerances. The cross- polarized (X-pol) component in the H-plane does not exceed −35 dBi.

The simulated far-field patterns of the four- and six-element antennas are depicted in Fig. 9. The nominal designs are expected to reach realized gain levels of 14 and 15.4 dBi at the center frequency, with indicated radiation efficiencies of 79% and 77%, respectively. This matches the expected gain difference of 1.4 dB based on the antenna dimensions, which indicates that the antenna scales efficiently. The four-element AiP achieves a peak side lobe level (SLL) of −10.7 dB, and the six-element design −12.1 dB.

Both antennas are expected to achieve a wide azimuthal field of view thanks to their E-plane half-power beamwidth (HPBW) of around 70°. In elevation, denoting the H-plane, the main beam is focused to a HPBWs of 14.4° and 10.1° for the four- and six-element design, respectively. Frequency scanning is limited to around ±4° for both designs within the 107-113 GHz operating bandwidth, with the beams scanning away from the feed for increasing frequency.

For both designs, the main beam at 110 GHz does not vary significantly due to the simulated manufacturing tolerances. However, the largest side lobe, which is radiated away from the feed, can vary by several decibels.

A five-element series-fed patch antenna design in a similar FOWLP technology was presented in [7]. In addition to the benefits of using a differential-style antenna, as mentioned in the previous sections, a performance comparison can be made between the two designs. A similar simulated −10 dB bandwidth of 5.7% around 140 GHz is reported, and a measured result of approximately 7.3% around 137 GHz. However, in [7], a beam offset from the broadside and a significantly lower peak realized gain of 12.5 dBi are reported, which can be attributed to the approximate half-wavelength element spacing of the design.

3.5. Realization

Fig. 10 shows the front- and backsides of a realized six-element sample, showing the backside RMS copper roughness that was measured to be 2.6 µm. The average thickness of the realized copper layer before the surface finish is 12.4 µm with a peak standard deviation of 0.82 µm. The copper thickness tended to increase radially from the center of the wafer, leading to slight under-etching at the edges of the wafer. As a result, a total of six four-element and seven six-element samples were successfully realized out of eight designed samples each. The three failed antenna samples were all caused by shorts and were located at the edge of the wafer.

After manufacturing, the etching tolerances were observed to be slightly higher than expected at a maximum variation of ±20 µm. The thickness of the real resin substrate was measured to be within a 225 to 250 µm range. These values are slightly outside of the ranges considered in the design process, but will be taken into account in the discussion of measurement results. It should be noted that manufacturing was done on a multi-project wafer without optimization to specific designs, which could be improved to achieve better tolerances and yield.

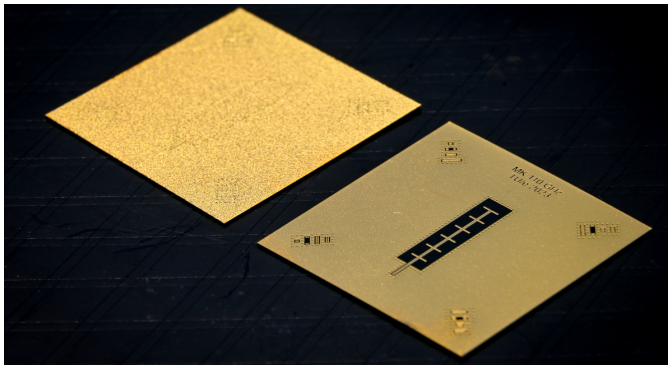

Figure 10: Realized samples of the six-element design. Sample size is 25×25 mm^2. The top-side metalization (shown right) features a considerably lower copper roughness than the bottom side (left). The structures in the corners are Thru-Reflect-Line (TRL) standards that are not considered in this work.

4. Measurements

4.1. Far-field patterns: mm-Wave anechoic chamber

Key to the measurement campaign of the presented D-band antenna samples is the novel mm-wave anechoic chamber that was developed in-house at TU/e [22]. Equipped with a Keysight vector network analyzer (VNA), the compact and mobile setup has an inside diameter of 1.10 m corresponding to approximately 400 wavelengths at 110 GHz. The chamber is a Faraday cage covered with absorbers to keep outside interference at a minimum.

As shown in Fig. 11, the antenna under test (AUT) is placed on a pedestal in the center of the compact spherical chamber. A rail-based reference antenna, in this case a pre-characterized WR-8 standard gain horn by Flann Microwave, can scan around the AUT to create a far-field pattern cut along the θ-axis between ±125° [33, 34]. Moreover, the entire spherical chamber can rotate 180° along the ϕ-axis to characterize an entire three-dimensional pattern. The reference antenna can move in the radial direction, and rotate to measure co- and cross-polarization.

The mm-wave anechoic chamber is equipped with a planar translation table that can move the center pedestal by up to 190 mm in the x- and y-directions for planar near-field scans. In addition, the translation table is equipped with a probe station allowing for up to 25 mm of precise movement on the x-, y- and z-axes. In this case, the AUT is placed on a second, rigid

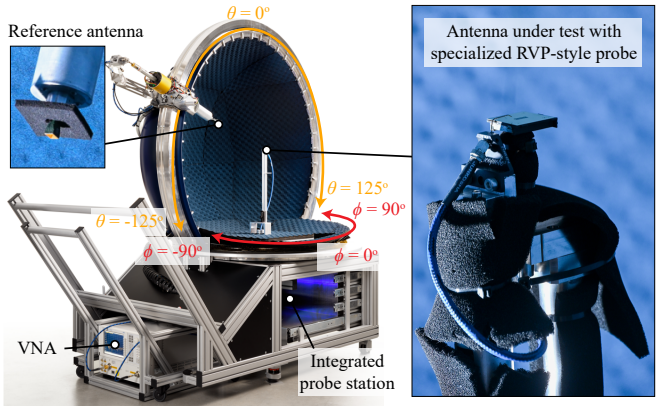

Figure 11: An overview of the millimeter-wave anechoic chamber (Half-open for illustration purposes).

pedestal that has been pre-centered. A 90-140 GHz extender from Virginia Diodes, Inc. (VDI) is mounted directly underneath the probe station, and the mm-wave signal is carried to the top of the pedestal by a WR-8 waveguide [35]. The reference antenna is connected to a mixer, also from VDI, to down-convert the received signal.

RF-probes can have a significant impact on the radiating performance of an antenna, especially at mm-wave frequencies [36]. This is due to parasitic radiation at the probe tips and reflections by the nearby bulky probe body. To minimize the disturbance caused by the body, a custom variation of Picoprobe's RVP-style probe introduced in [37] is used that positions the probe body below the antenna as shown in Figs. 11 and 12. The available probes have 100 µm-pitch ground-signal (GS) and signal-ground (SG) tips, and 1.0 mm RF-connectors that are rated for mode-free operation up to 110 GHz.

4.2. Input reflection

The antenna input reflection was measured inside the mm-wave anechoic chamber with the aforementioned GS and SG probes and the probe station, using a top-mounted camera for alignment and landing. As the mm-wave anechoic chamber does not support multiprobe measurements at the time of writing, Thru-Reflect-Line (TRL)-calibration was not possible. For this reason, the setup was calibrated at the tip of the probe with short, open, and 50 Ω load (SOL) standards on a calibration substrate placed on the antenna pedestal before measurement. It should be noted that the 1.0 mm RF-connector is expected to limit the measurement accuracy above 110 GHz, and that the transitions and flexibility due to the 1.0 mm connector and cable will add to the overall loss and uncertainty of the measurement system.

4.3. Realized gain

The strategy used to characterize the realized gain level is described in [38]. The method is based on the Friis transmission equation, given by [39]

$$\frac{P_{\mathrm{Rx}}}{P_{\mathrm{Tx}}} = G_{\mathrm{Tx}} G_{\mathrm{Rx}} \left(\frac{\lambda_0}{4\pi R}\right)^2 \times L_{\mathrm{tl}}, \text{ where } R > \frac{2D_{\mathrm{a}}^2}{\lambda_0}. \qquad (2)$$

In this equation, $(P_{\mathrm{Rx}}/P_{\mathrm{Tx}})$ is the power transmission ratio S_{21} that can be measured with the two-port VNA, although a loss factor L_{tl} must be accounted for. G_{Tx} and G_{Rx} denote the realized gains of the transmitting AUT and receiving reference antenna, respectively. Moreover, R denotes the distance between the amplitude centers of the two antennas that must exceed the far-field criterion determined by the aperture dimension of the antenna D_{a}. For the six-element AiP, D_{a} is taken as the diagonal of the $L_{\mathrm{a}} \times W_{\mathrm{a}}$ aperture, and for a peak measurement frequency of 120 GHz the farfield distance is around 120 mm.

A second horn antenna with known realized gain is placed in the AUT position. After positioning the reference horn antenna directly above and taking a series of transmission measurements while varying the radial distance between the two antennas from 130 to 190 mm, the phase center distance R between the antennas is determined by fitting the Friis equation. With all other variables known, the total power loss in waveguides, cables, and transitions L_{tl} can be determined.

After characterizing the setup losses, the process can be repeated for the AUTs to determine their realized gain relative to the reference horn antenna.

4.4. Modeling of probe influence

Despite the bulk of its body being outside the field of view of the AiP, the housing of the GS RF-probe used in the mm-wave anechoic chamber was expected to have a considerable influence on the radiated measurement results.

The parasitic radiation of the probe was characterized by landing on the 50 Ω load calibration standard and measuring the far-field pattern and the realized gain using the methods described in this section. Based on the measurements, this parasitic radiation is expected to limit the reliably measurable realized AUT gain, or null depth, to ≥ -15 dBi. This was considered to be sufficiently low to reliably measure the main beam and primary side lobes, but the interfering radiation causes ripples in the lower side lobes and X-pol patterns. Methods to remove these ripple effects of probe radiation from antenna pattern measurements exist and have been explored in [40], although these methods are not without shortcomings. In [40], a highly repeatable and accurate probe and antenna positioning in the order of micrometers is described for a 28 GHz scenario, which cannot be replicated in the mm-wave anechoic chamber. Moreover, the 100 Ω antenna interface impedance must be replicated by a nonradiating test structure to accurately measure the probe radiation with the correct loading conditions. As the additional measurement and processing efforts outweighed the benefits of reducing the ripple at approximately -15 dBi of realized gain, no de-embedding of the probe radiation pattern was performed.

Moreover, the GS or SG configuration is expected to cause an asymmetry in the antenna excitation. A balun could help avoid this, but it would possibly introduce additional parasitic radiation and result in additional losses to de-embed, requiring additional test structures. Ideally, an antenna design intended for a high degree of integration would be measured as part of a fully packaged system, leading to several practical chal-

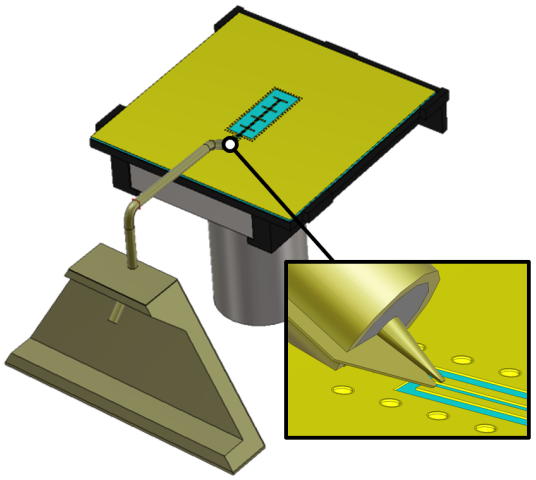

Figure 12: CST model of the four-element AiP including metal pedestal, plastic holder, and the GS-probe used for far field measurements.

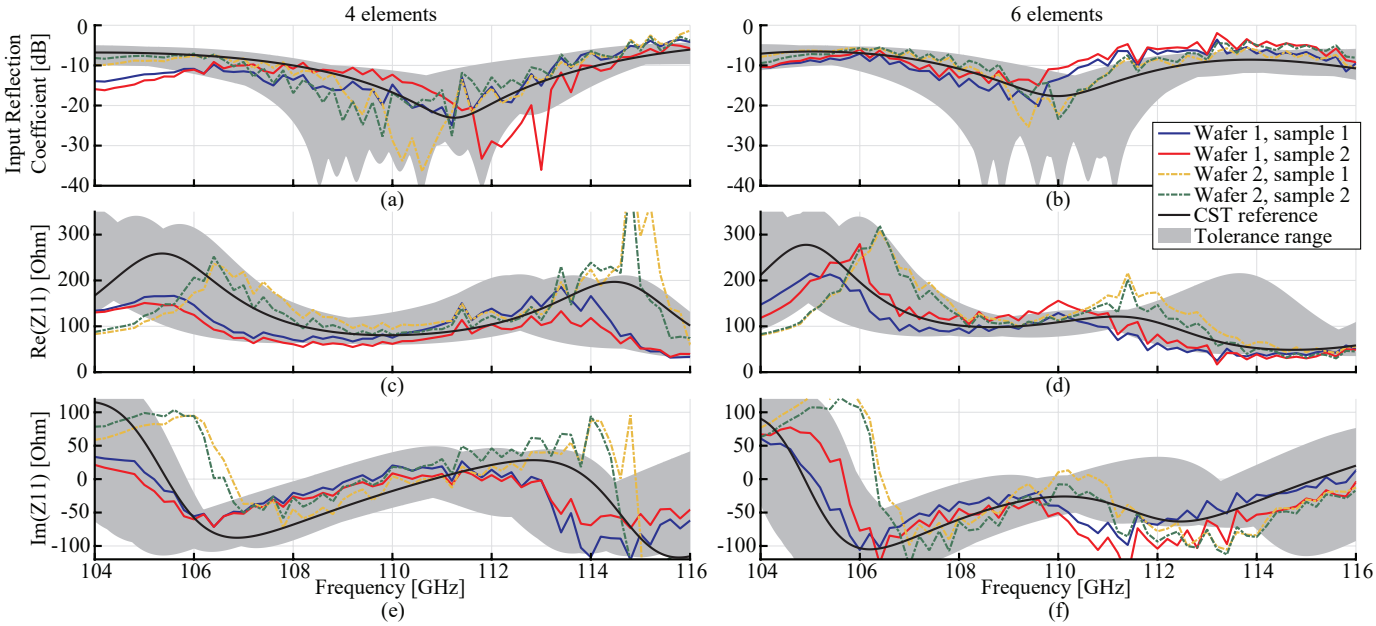

Figure 13: Measured input reflection magnitude for a 100 Ω reference impedance (a-b), and complex antenna impedance Z_{11} (c-f) of the four-element (a,c,e) and six-element (b,d,f) antennas. A range of simulation results based on manufacturing and measurement tolerances is shaded grey. The CST reference includes the feed point offset, the measured decreased substrate thickness, and the increased copper thickness. The probe was not co-simulated in this case.

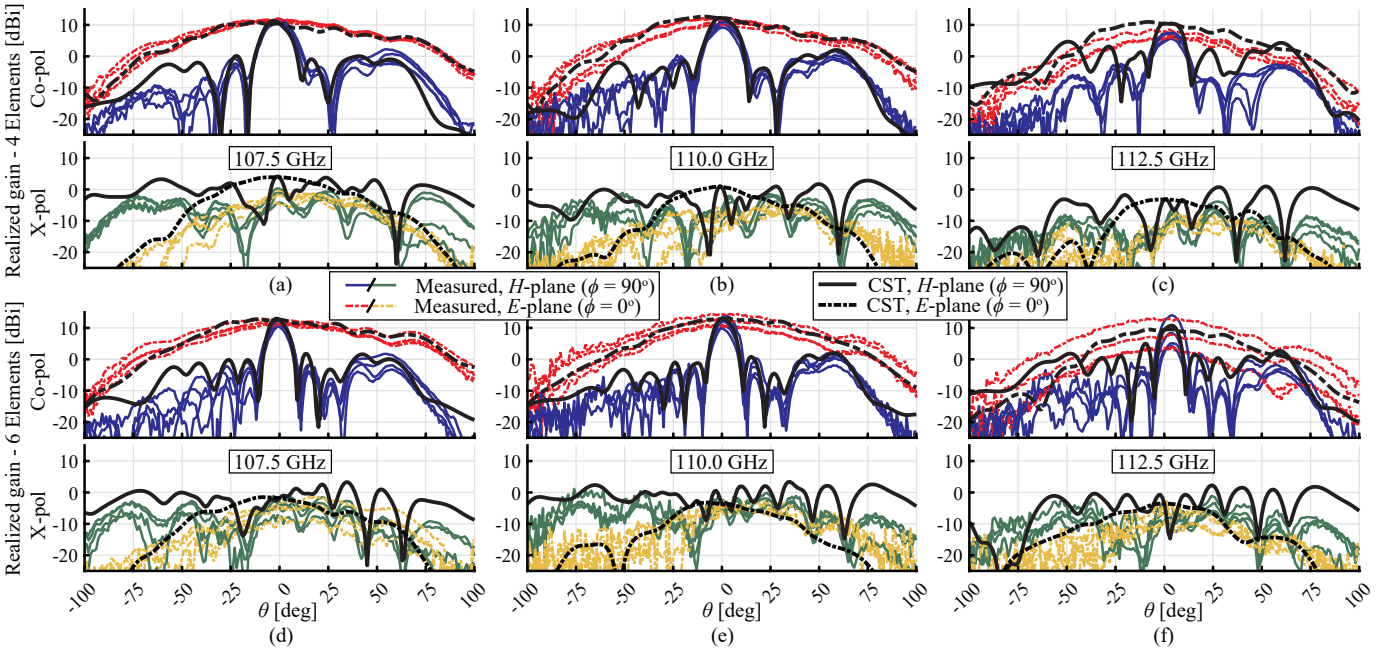

Figure 14: Measured realized-gain patterns of four four-element (a-c) and four six-element (d-f) samples, two samples per wafer for both designs. The plots show the co-polarized (Co-pol) and cross-polarized (X-pol) patterns for 107.5 GHz (a,d), 110 GHz (b,e), and 112.5 GHz (c,f). Results from CST simulations of the AiPs without manufacturing tolerances and including a GS-probe as depicted in Fig. 12 are included for reference.

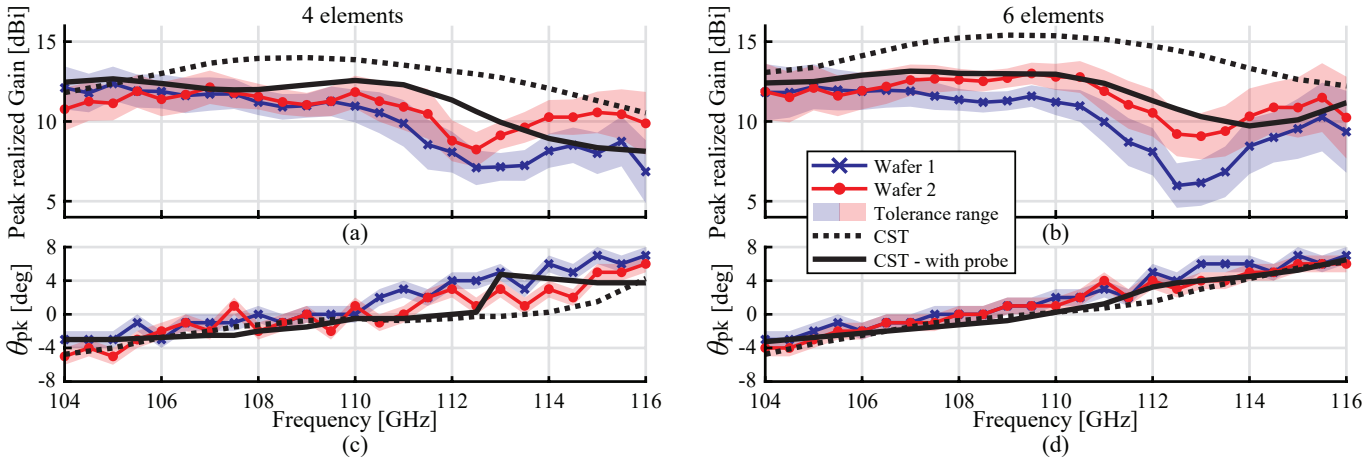

Figure 15: Measured peak realized gain values (a-b) and peak gain direction θ_{pk} (c-d) for the four-element (a,c) and six-element (b,d) designs. The tolerance ranges caused by measurement inaccuracies, including angular misalignment and probe positioning, are indicated. CST simulations of the AiPs without and including a GS-probe as depicted in Fig. 12 are included for reference.

lenges described in [41]. Instead, in this work, a probe model was co-simulated in CST to characterize its influence on the measurement results as depicted in Fig. 12.

5. Results

5.1. Input reflection and impedance

The measured input reflection parameters and impedances of the four- and six-element AiPs are shown in Figs. 13a-f.

The measurements indicated a significant sensitivity of the measured input reflection on the exact placement of the probe. Whilst the original model in CST was based on a discrete probe at the tips of the input transmission line, the probe position can be up to approximately 100 µm away from the edge. This forms a capacitive stub that de-tunes the antenna and shifts the resonance frequency. In an integrated module the probe will not be considered, but in its stead the misalignments and drilling variations of the layer transitions between the RF IC and the antenna must be accounted for.

Moreover, initial material characterization was performed with an accuracy of up to ±3% in the dielectric permittivity, which could account for a shift in resonance frequency of up to 1 GHz or less than 1% of the designed frequency. From the results in Fig. 13, a variation can be discerned between the samples in wafers 1 and 2, whilst the sample pairs within each wafer are more consistent. Ongoing research on the characterization of material properties and tolerances beyond 100 GHz of the FOWLP technology is expected to reduce manufacturing variations in the future.

The measured variations in probe position, dielectric constant, etching, and substrate thickness were considered to simulate the ranges depicted in grey in Fig. 13.

5.2. Far-field radiation patterns

The measured radiation pattern cuts in the E- ($\phi = 0°$) and H-planes ($\phi = 90°$) are shown in Fig. 14 for 107.5, 110 and 112.5 GHz. The realized gain measurements at broadside, shown in Fig. 15, were used to re-normalize the far-field pattern measurements. The patterns show excellent agreement with simulations, with better null and main beam alignment than examples from other works such as [7, 21], particularly at 107.5 and 110 GHz. The CST reference is based on the nominal design parameters, with the GS probe tips located at 75 µm from the start of the transmission line. Particularly the asymmetric co-polarized E-plane ripple and the cross-polarized H-plane pattern, both being absent from the nominal simulation without RF-probe, match well between simulation and measurement.

In [36], a 'trueness' parameter T is defined to quantify the level of agreement between measurements and a reference:

$$T(f) = \frac{1}{N_\theta} \sum_{n_\theta=1}^{N_\theta} \left(\frac{|R_n(f)|}{|R_n(f) - M_n(f)| + |R_n(f)|} \right) \cdot 100\% \quad (3)$$

R_n and M_n denote the reference and measured values at given measurement point n_θ, respectively. This equation describes the absolute distance from a certain value to a reference, where 100% denotes a complete agreement and 0% denotes complete disagreement. The resulting trueness values of the far-field patterns are depicted in Fig. 16, where the measured and simulated patterns are normalized to their respective peak values. It is apparent that the inclusion of the probe in the reference simulation results in a notable improvement in agreement of 10 to 15 percent points.

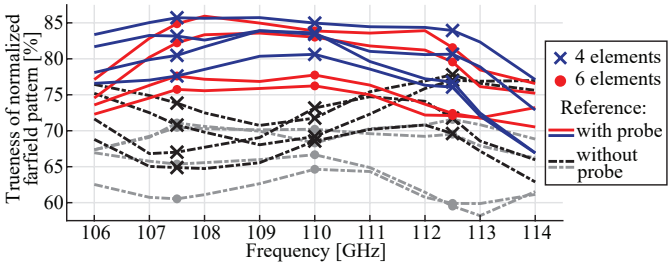

Figure 16: Trueness of the measured radiation patterns in Fig. 14, with respect to reference CST simulations with and without the RF-probe.

Table 4: Comparison of differential D-band antennas from literature.

Design	Elements	f_c [GHz]	Size $[\lambda_0 \times \lambda_0]$	Gain [dBi]	η_{ant} [%]	BW [%]	Source
On-chip dipoles	4×4	110	2.0×2.0	13.5	45	7.3	[42]
Wafer-level rhombic grid array	8	120	1.5×1.1	11	-	5	[2]
"	43	120	5.5×2.0	15.5	75	4.9	[21]
Series-fed patch antenna on PCB	1×8	123.5	5.7×0.5	13	90	5.7	[43]
End-fire dipole array in metal fixture	1×8	145	3.9×0.8	14.7	70	41.4	[11]
Wafer-level patch arrays with balun:	2×2	139.5	2.26×2.26	11	65	22.2	[13]
"	2×4	135.9	4.0×2.7	12.7	54	35.5	[14]
"	2×4	137.7	4.1×2.8	13.7	45.2	32.7	[15]
Wafer-level series-fed dipole array	1×4	110	1.1×2.9	14	79	5.5	This work
"	1×6	110	1.1×4.4	15.4	77	5.9	
"	4×6	110	2.6×4.7	18.5	74	4.5	

Definitions: f_c: center frequency. λ_0: free-space wavelength at f_c. η_{ant}: antenna efficiency. BW: bandwidth.

5.3. Realized Gain

In Fig. 15, the measured and simulated peak gain levels and pointing angles are depicted between 104 and 116 GHz. The tolerance range is the cumulative result of a ±1° antenna misplacement, the landing position of the probe, and the maximum variations in the measurement results of the two-antenna method described in Section 4-C. The range remains within ±1 dB within 107.5 and 100 GHz, but reaches to ±1.5 dB between 100 and 112.5 GHz.

At respective peak levels of 12.0 and 12.9 dBi for the four- and six-element, the realized gain values at 110 GHz are significantly lower than the simulated values without a probe. As indicated by the simulations that include the RF-probe, this can largely be attributed to a mismatch caused by the probe's 50 Ω interface impedance, ripple induced by the parasitic probe radiation, and a slightly offset main beam direction due to the asymmetric GS excitation.

Beyond 110 GHz, the measured peak values start to deviate from the CST simulations with offsets that cannot be explained by alignment tolerances alone. Increasing sensitivity to measurement variations, caused by the increasing impedance mismatch to the 50 Ω probe beyond 110 GHz as shown in Figs. 13c-f, is a probable cause for the wider deviations around 112.5 GHz seen in Figs. 14f and 15.

5.4. State-of-the-art comparison

The overview of the reported realized gain performance in Fig. 1 was re-made to focus on the differential designs in Fig. 17. The performances presented in this work are also included in the graph and are considered corroborated by the probe-based measurements due to the agreement to within 1 dB with simulations. They are marked with '4' and '6' in Fig. 17 to denote their element counts. Note that [11] and [13–15] are differential radiators but have waveguide-based and single-ended interfaces, respectively. Nevertheless, they have been included in Fig. 17 to expand the comparison with more recently published examples.

The aperture dimensions $L_a \times W_a$ were taken as the antenna area, which is larger than the radiating dipole structure. Still, the antennas presented in this work outperform the gain-versus-area trends of other differential PCB-, chip- and package-based

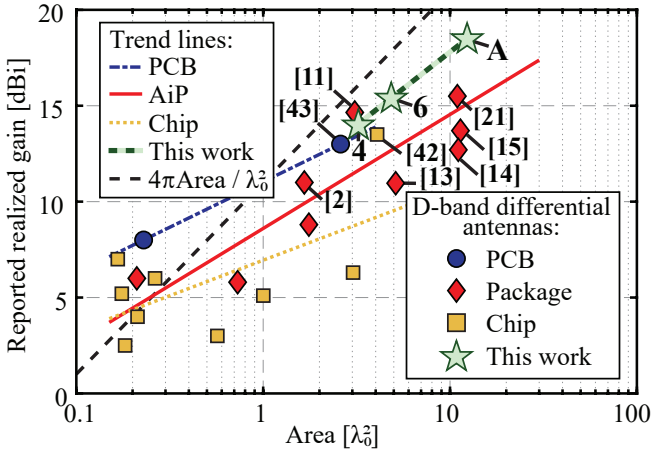

Figure 17: Overview of reported realized gain performances of differential D-band antennas from literature. Adapted from [6] and includes the following works: [2, 11, 13–15, 21, 42–52]. The antennas presented in this work are labeled as '4,' '6' (denoting element count) and 'A' (array, see Fig. 18).

antennas in the D band. The comparatively high rate of gain increase with size indicates a scalable and low-loss performance of the antenna design and the used FOWLP technology. The only other high-gain AiP design that outperforms the gain-area ratio is [11], which is a corporate-fed end-fire dipole array in a metal fixture. This is a promising structure with the possibility to extend towards a 2-dimensional scanning array, but not directly implementable as a low-profile PCB-mounted package as depicted in Fig. 2.

The limited subset of integrated antennas with over 10 dBi of reported realized gain is listed in more detail in Table 4. The presented AiP designs outperform the chip- and PCB-based antennas from [42] and [43] in terms of realized gain per unit area. Notable among the differential AiPs are the 120 GHz 8-element and 43-element rhombic arrays from [2] and [21], respectively. These designs are implemented in an embedded wafer level ball grid array (eWLB) technology, and report 11 and 15.5 dBi of realized gain respectively. Compared to these designs, the

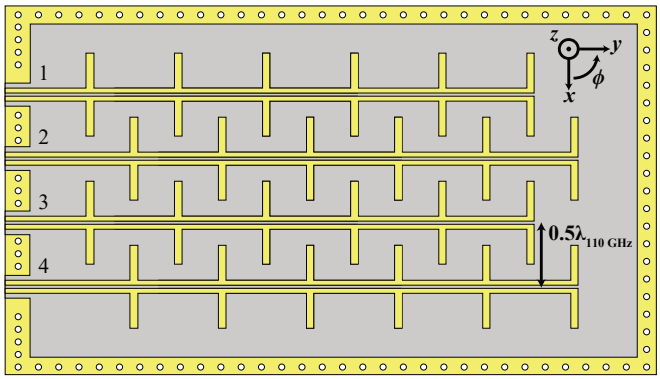

Figure 18: Design of the four-by-six-element array. The surrounding substrate and metal extend to 25×25 mm.

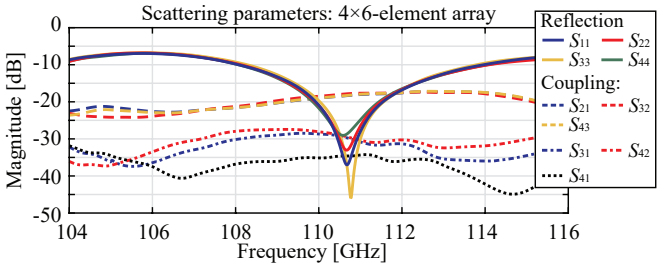

Figure 19: Simulated scattering parameters of the four-by-six element array.

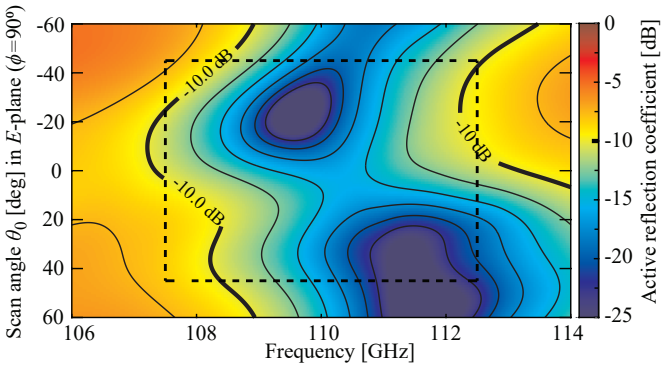

Figure 20: The active reflection coefficient magnitude of element 2 as indicated in Fig. 18, based on a uniform excitation.

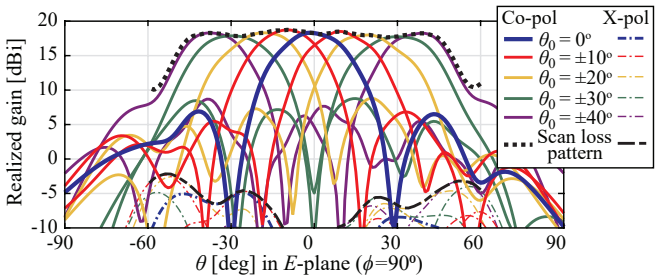

Figure 21: The E-plane realized-gain patterns at 110 GHz for scan angles up to 40° from broadside, of the array in Fig. 18.

multilayer capability offered by the FOWLP technology used in this work enables a greater degree of design freedom and positioning of the antenna on top of the overmolded RF IC.

6. Outlook: Electronically Scanned Array-Antenna-in-Package

Unlike the fixed-gain rhombic arrays of [2] and [21], the series-fed elements presented in this work can be configured in a linear array. This allows further scalability to increase the gain, improve the angular resolution, and enable E-plane beam-steering. In this array configuration, each series-fed array would be connected to a mm-wave beamforming circuit to provide amplification and 360-degree phase control range. Recent examples of beamforming circuits operating near the frequency range include [53] and [54].

Without any adjustments to the element design, four six-element antennas were combined in an array with a half-wavelength element spacing in the x-direction and a staggered grid, as shown in Fig. 18. The feed structure and line length L_{tl} are not shown but identical to the design in Fig. 3. Based on the scattering (S)-parameters from full-wave simulations in CST, depicted in Fig. 19, the isolation between adjacent elements is expected to be at least 17.2 dB within the 107.5-112.5 GHz operating bandwidth. The minimum isolation between elements that are two x-spacings apart is 27 dB, and the outer elements are isolated by at least 34 dB.

The simulated S-parameters are combined in MATLAB to produce the active reflection coefficient (ARC) for element m using the definition

$$\mathrm{ARC}_m(\theta_0) = \sum_{n=1}^{N_{\mathrm{ant}}} S_{mn} \frac{|\mathrm{a}_n| e^{\mathrm{j}\varphi_n}}{|\mathrm{a}_m| e^{\mathrm{j}\varphi_m}}, \tag{4}$$

where $|\mathrm{a}_n|$ and φ_n are the excitation amplitude and phase of element n, respectively, and N_{ant} is the total number of driven antenna elements. The resulting ARC for element 2, assuming uniform excitation and perfect phase shifts for the given scan angle θ_0, is shown in Fig. 20 for all combinations of scan angle and operating frequency. The broadside –10 dB bandwidth spans between 107.5 and 112.5 GHz.

The far-field radiation patterns of the scanning array were obtained by simultaneous excitation of the four elements in full-wave simulation, with the required phase settings for a given scan direction determined at 110 GHz. The results are depicted in Fig. 21. The achievable scan range is not limited by the ARC, which would indicate a scan range beyond ±60° as shown in Fig. 20, but rather by the E-plane radiation pattern of the elements. The peak-gain scan pattern of the four-by-six array varies between 18.6 and 17.6 dBi, before dropping off rapidly beyond ±45° as depicted in Fig. 21. The side-lobe levels range from –11.5 dB at broadside to –9.5 dB at the furthest scan angles, which can be reduced through further expansion of the array and applying amplitude tapering. The cross-polarization ratio does not exceed 20 dB within the ±45° scan range.

The realized-gain performance of the simulated array was included in Table 4 and Fig. 17, and extends the gain-versus-area trend of this work. Based on the gain-scalability and excel-

lent scanning performance indicated by this feasibility study, combined with the possibility of close integration with beamforming electronics, the scanning Array-Antenna-in-Package (AAiP) implementation of the presented design is a promising future outlook for automotive radars operating in the D-band.

7. Conclusion

The design of a D-band differential reflector-backed dipole array antenna in a FOWLP technology has been presented. The four- and six-element series-fed designs operate with a 6% bandwidth around 110 GHz and serve as proofs of concept of highly integrated radar components beyond 100 GHz.

Based on a scalability analysis, the designs can be scaled up to 9 elements for gain enhancement to 16 dBi without a need for re-tuning the input match for a bandwidth exceeding 107-112 GHz. Within this bandwidth, beam squint will not steer the beam beyond its half-power level from broadside.

The antennas were characterized through probe-based measurements in a state-of-the-art anechoic measurement chamber. The influence of the probe on the antenna performance was determined through full-wave simulations, resulting in improvements in agreement between measurements and simulations of 10 to 15 percent points. The realized gain and beam squint performance were corroborated by measurements as well. The presented antenna performance represents an advancement over the limited number of previously published package-based differential antennas operating at the D-band, demonstrating excellent gain-over-area performance beyond the state-of-the-art. Moreover, a feasibility study into the expansion of this design into an E-plane scanning array indicated excellent beam-scanning performance up to $\pm 45°$, and a further scalability of achievable gain beyond what can practically be achieved by a single series-fed element.

The broadside radiation perpendicular to the PCB plane, combined with the scalability of the design as highlighted in Sections III.C and V.D, and the potential to expand towards a scanning array sets the design apart from other previously published works in this frequency range. Based on the efficient scalability and the achievable manufacturing tolerances, the FOWLP technology is considered a promising candidate to realize highly integrated front-end modules for the beyond-100 GHz era of automotive radars.

Acknowledgment

This document is a result of the NEXTPERCEPTION project (www.nextperception.eu), which is jointly funded by the European Commission and national funding agencies under the ECSEL joint undertaking. Part of the work described in this document is also co-funded by the PENTA-EURIPIDES 2021 project InnoStar (www.project-innostar.com).

The authors acknowledge and thank Noah Reniers of Reniers Mechatronics for his help with the antenna measurements in the mm-wave anechoic chamber.

References

[1] J. Edstam, J. Hansryd, S. Carpenter, T. Emanuelsson, Y. Li, and H. Zirath, "Microwave backhaul evolution - reaching beyond 100 GHz," 2017.

[2] M. Furqan, F. Ahmed, R. Feger, K. Aufinger, W. Hartner, and A. Stelzer, "A SiGe-based fully-integrated 122-GHz FMCW radar sensor in an eWLB package," *International Journal on Microwave and Wireless Technologies*, vol. 9, no. 6, p. 1219–1230, 2017.

[3] H. J. Ng, M. Kucharski, W. Ahmad, and D. Kissinger, "Multi-purpose fully differential 61- and 122-GHz radar transceivers for scalable MIMO sensor platforms," *IEEE Journal of Solid-State Circuits*, vol. 52, no. 9, pp. 2242–2255, 2017.

[4] M. Köhler, J. Hasch, H. Bloecher, and L.-P. Schmidt, "Feasibility of automotive radar at frequencies beyond 100 GHz," *International Journal on Microwave and Wireless Technologies*, vol. 5, Feb 2013.

[5] V. Vidojkovic *et al.*, "RF and mm-wave systems and circuits for communications and sensing," in *2023 58th International Scientific Conference on Information, Communication and Energy Systems and Technologies (ICEST)*, pp. 83–92, 2023.

[6] M. de Kok, A. B. Smolders, and U. Johannsen, "A review of design and integration technologies for D-band antennas," *IEEE Open Journal on Antennas and Propagation*, vol. 2, pp. 746–758, 2021.

[7] T. H. Le, O. Schwanitz, I. Ndip, F. Mueller, T. Braun, and M. Schneider-Ramelow, "Design, fabrication and measurement of FOWLP-based series-fed antennas for 6G D-band MIMO applications," in *2022 IEEE 9th Electronics System-Integration Technology Conference (ESTC)*, pp. 593–596, 2022.

[8] S. Erdogan and M. Swaminathan, "D-band quasi-Yagi antenna in glass-based package," in *2021 IEEE MTT-S International Microwave and RF Conference (IMARC)*, pp. 1–4, 2021.

[9] A. Lamminen *et al.*, "D-band antenna and array designs for 5G applications," in *2023 Joint European Conference on Networks and Communications & 6G Summit*, pp. 597–601, 2023.

[10] S. Zhao, Y. Xu, and Y. Dong, "An LTCC-based antenna array for D-band terahertz communication," *IEEE Antennas and Wireless Propagation Letters*, vol. 22, no. 6, pp. 1491–1495, 2023.

[11] Y. W. Kim, Y. K. Koh, and M. Kim, "Microstrip array antennas packaged in metal fixture for 150 GHz beamforming applications," *IEEE Antennas and Wireless Propagation Letters*, vol. 23, no. 3, pp. 1055–1059, 2024.

[12] D. Wang and K.-D. Xu, "Dual-band substrate integrated waveguide cavity-backed antenna based on LTCC in D-band," in *2022 International Applied Computational Electromagnetics Society Symposium*, 2022.

[13] X. Wang, G. Xiao, L. Yang, H. Li, and Q. Xu, "Broadband D-band patch antenna array in wafer-level package based on BCB process," *IEEE Open Journal of Antennas and Propagation*, vol. 3, pp. 1172–1179, 2022.

[14] X. Wang, G. Xiao, and H. Cheng, "A broadband D-band cavity-backed coupled-feed patch antenna in wafer level package," in *2022 IEEE MTT-S International Wireless Symposium (IWS)*, vol. 1, pp. 1–3, 2022.

[15] X. Wang, G. Xiao, B. Zhao, Y. Huang, and Q. Xu, "A broadband D-band cavity-backed coupled-feed patch antenna in wafer-level package based on heterogeneous integrations," *IEEE Transactions on Antennas and Propagation*, vol. 72, no. 8, pp. 6298–6308, 2024.

[16] Franhofer IZM, "Main web page," 2024. [Online]. Available: https://www.izm.fraunhofer.de.

[17] T. Braun *et al.*, "Development of a scalable AiP module for mmWave 5G MIMO applications based on a double molded FOWLP approach," in *2021 IEEE 71st Electronic Components and Technology Conference (ECTC)*, pp. 2009–2015, 2021.

[18] M. Zhao, "Differential interfaces improve performance in RF transceiver designs," *Analog Dialogue*, vol. 45, Jul 2011.

[19] M. Furqan, F. Ahmed, K. Aufinger, and A. Stelzer, "A D-band fully-differential quadrature FMCW radar transceiver with 11 dBm output power and a 3-dB 30-GHz bandwidth in SiGe BiCMOS," in *2017 IEEE MTT-S International Microwave Symposium*, pp. 1404–1407, 2017.

[20] M. de Kok, P. A. Escobari Vargas, E. Meyer, F. Müller, T. Braun, A. C. F. Reniers, and U. Johannsen, "A differential series-fed dipole array for D-band sensing in wafer level package technology," in *2025 19th European Conference on Antennas and Propagation (EuCAP)*, 2025.

[21] M. Furqan, F. Ahmed, and A. Stelzer, "A SiGe 122-GHz FMCW radar sensor with 21.5 dBm EIRP based on a 43-element antenna array in an eWLB package," in *IEEE MTT-S International Conference on Microwaves for Intelligent Mobility*, pp. 1–4, 2018.

[22] A. C. F. Reniers, A. Hubrechsen, G. Federico, L. A. Bronckers, and A. B. Smolders, "Spherical mm-wave anechoic chamber for accurate far-field radiation pattern measurements," in *2022 52nd European Microwave Conference (EuMC)*, pp. 318–321, 2022.

[23] T. Braun *et al.*, "Fan-out wafer level packaging for 5G and mm-Wave applications," in *2018 International Conference on Electronics Packaging and iMAPS All Asia Conference (ICEP-IAAC)*, pp. 247–251, 2018.

[24] P. A. Escobari Vargas, *Packaging Technology Characterization for 5G Antenna-in-Package and Filter-in-Package application*. EngD thesis, Eindhoven University of Technology, Feb. 2024.

[25] Dassault Systèmes, "CST Studio Suite," 2024. [Online]. Available: https://www.3ds.com/products/simulia/cst-studio-suite.

[26] W. Menzel, "Antennas in automobile radar," in *Handbook of Antenna Technologies* (Z. N. Chen, ed.), pp. 1–22, Springer Singapore, 2014.

[27] U. Johannsen, A. B. Smolders, A. C. F. Reniers, A. R. V. Dommele, and M. D. Huang, "Integrated antenna concept for millimeter-wave front-end modules in proven technologies," in *2012 6th European Conference on Antennas and Propagation (EuCAP)*, pp. 2560–2563, 2012.

[28] H. Wang and I. Park, "Series-fed printed dipole array antenna," in *2018 11th Global Symposium on Millimeter Waves (GSMM)*, pp. 1–3, 2018.

[29] H. Wang, K. E. Kedze, and I. Park, "A high-gain and wideband series-fed angled printed dipole array antenna," *IEEE Transactions on Antennas and Propagation*, vol. 68, no. 7, pp. 5708–5713, 2020.

[30] H. Wang and I. Park, "Coplanar strip line-fed series dipole array antenna for high-gain realization," *IEEE Transactions on Antennas and Propagation*, vol. 69, no. 8, pp. 5106–5111, 2021.

[31] R. C. Hansen, "Array feeds," in *Phased Array Antennas*, pp. 164–188, Wiley, 1998.

[32] C. A. Balanis, "Antenna vector effective length and equivalent areas," in *Antenna Theory: Analysis and Design*, pp. 81–86, Wiley, 4 ed., 2016.

[33] Flann Microwaves, *Standard gain horn series 240*, Jan 2024. [Online]. Available: https://flann.com/products/antennas/standard-gain-horns-series-240/".

[34] P. Yadav, L. A. Bronckers, and A. C. F. Reniers, "Uncertainties in the estimation of the gain of a standard gain horn in the frequency range of 90 GHz to 140 GHz," in *2024 European Conference on Antennas and Propagation*, 2024. Accepted for publication.

[35] Virginia Diodes, Inc., *VNA Extender: WR8.0-VNAX*, Jan 2024. [Online]. Available: https://www.vadiodes.com/index.php/en/products/vector-network-analyzer?id=851.

[36] A. Reniers, *Uncertainties in millimeter-wave antenna design, modeling and characterization: The observer effect*. Phd thesis, Eindhoven University of Technology, dept. of Electrical Engineering, May 2022.

[37] A. C. F. Reniers, A. R. van Dommele, A. B. Smolders, and M. H. A. J. Herben, "The influence of the probe connection on mm-wave antenna measurements," *IEEE Transactions on Antennas and Propagation*, vol. 63, no. 9, pp. 3819–3825, 2015.

[38] A. J. van den Biggelaar *et al.*, "Accurate gain measurement technique for limited antenna separations," *IEEE Transactions on Antennas and Propagation*, vol. 69, no. 10, pp. 6772–6782, 2021.

[39] H. Friis, "A note on a simple transmission formula," *Proceedings of the IRE*, vol. 34, no. 5, pp. 254–256, 1946.

[40] Z. Zheng and Y. Zhang, "Characterization and de-embedding of wafer probe radiation for integrated antenna measurements," *IEEE Transactions on Antennas and Propagation*, vol. 71, no. 12, pp. 9440–9453, 2023.

[41] A. Hubrechsen and A. van den Biggelaar, "Over-the-air techniques for measuring integrated RF electronics and antennas," *Microwave Journal*, Jan 2024.

[42] W. Shin, B. Ku, O. Inac, Y. Ou, and G. M. Rebeiz, "A 108–114 GHz 4 $\times$4 Wafer-Scale Phased Array Transmitter With High-Efficiency On-Chip Antennas," *IEEE Journal of Solid-State Circuits*, vol. 48, no. 9, pp. 2041–2055, 2013.

[43] R. Hasan, W. A. Ahmed, J. Lu, H. J. Ng, and D. Kissinger, "F-Band Differential Microstrip Patch Antenna Array and Waveguide to Differential Microstrip Line Transition for FMCW Radar Sensor," *IEEE Sensors Journal*, vol. 19, no. 15, pp. 6486–6496, 2019.

[44] A. Bunea *et al.*, "160 GHz silicon micromachined folded slot antenna array," in *2012 Asia Pacific Microwave Conference (APMC)*, pp. 896–898, 2012.

[45] A. Bisognin *et al.*, "D-band quasi-yagi antenna in IPD process," in *2013 7th European Conference on Antennas and Propagation (EuCAP)*, pp. 330–331, 2013.

[46] B. P. Ginsburg, S. M. Ramaswamy, V. Rentala, E. Seok, S. Sankaran, and B. Haroun, "A 160 GHz Pulsed Radar Transceiver in 65 nm CMOS," *IEEE Journal of Solid-State Circuits*, vol. 49, no. 4, pp. 984–995, 2014.

[47] W. T. Khan *et al.*, "A D-Band micromachined end-fire antenna in 130-nm SiGe BiCMOS technology," *IEEE Transactions on Antennas and Propagation*, vol. 63, no. 6, pp. 2449–2459, 2015.

[48] D. Dancila, V. Valenta, A. Bunea, D. Neculoiu, H. Schumacher, and A. Rydberg, "Differential microstrip patch antenna as feeder of a hyper-hemispherical lens for F-band MIMO radars," in *ESA Workshop on Millimetre-Wave Technology and Applications*, pp. 1–4, 2016.

[49] F. Ahmed, M. Furqan, and A. Stelzer, "120-GHz and 240-GHz broadband bow-tie antennas in eWLB package for high resolution radar applications," in *48th European Microwave Conference (EuMC)*, pp. 1109–1112, 2018.

[50] W. Ahmad, M. Kucharski, H. Ng, and D. Kissinger, "A compact efficient D-band micromachined on-chip differential patch antenna for radar applications," in *IEEE International Symposium on Antennas and Propagation and USNC-URSI Radio Science Meeting*, pp. 2201–2202, 2019.

[51] W. A. Ahmad, M. Kucharski, A. Di Serio, H. J. Ng, C. Waldschmidt, and D. Kissinger, "Planar highly efficient high-gain 165 GHz on-chip antennas for integrated radar sensors," *IEEE Antennas and Wireless Propagation Letters*, vol. 18, no. 11, pp. 2429–2433, 2019.

[52] A. Visweswaran *et al.*, "A 145GHz FMCW-radar transceiver in 28nm CMOS," in *IEEE International Solid-State Circuits Conference - (ISSCC)*, pp. 168–170, 2019.

[53] P. Magnée *et al.*, "Full antenna in package solution for 100GHz 6G infrastructure, in 140nm SiGe BiCMOS technology," in *2024 IEEE BiCMOS and Compound Semiconductor Integrated Circuits and Technology Symposium (BCICTS)*, pp. 177–180, 2024.

[54] Y. Zhang, K. Vaesen, G. Mangraviti, S. Park, Z. Zong, P. Wambacq, and G. Gramegna, "A 56Gb/s zero-IF D-band transmitter for a beamformer in 22nm FD-SOI," in *2024 IEEE Radio Frequency Integrated Circuits Symposium (RFIC)*, pp. 347–350, 2024.